Investigation of axial-injection end-burning hybrid rocket motor regression

Yuji Saito[*1], Toshiki Yokoi[1], Lukas Neumann[2], Hiroyuki Yasukochi[3],
Kentaro Soeda[3], Tsuyoshi Totani[4], Masashi Wakita[4] and Harunori Nagata[4a]

[1]*Graduate school of Engineering, Hokkaido University, Japan*
[2]*Faculty of Engineering, Technical University of Berlin, Germany*
[3]*Institute for Photon Science and Technology, The University of Tokyo, Japan*
[4]*Faculty of Engineering, Hokkaido University, Japan*

Abstract. The axial-injection end-burning hybrid rocket proposed twenty years ago by the authors recently recaptured the attention of researchers for its virtues such as no ξ (oxidizer to fuel mass ratio) shift during firing and good throttling characteristics. This paper is the first report verifying these virtues using a laboratory scale motor. There are several requirements for realizing this type of hybrid rocket: 1) high fuel filling rate for obtaining an optimal ξ; 2) small port intervals for increasing port merging rate; 3) ports arrayed across the entire fuel section. Because these requirements could not be satisfied by common manufacturing methods, no previous researchers have conducted experiments with this kind of hybrid rocket. Recent advances in high accuracy 3D printing now allow for fuel to be produced that meets these three requirements. The fuel grains used in this study were produced by a high precision light polymerized 3D printer. Each grain consisted of an array of 0.3 mm diameter ports for a fuel filling rate of 98% .The authors conducted several firing tests with various oxidizer mass flow rates and chamber pressures, and analysed the results, including ξ history, using a new reconstruction technique. The results show that ξ remains almost constant throughout tests of varying oxidizer mass flow rates, and that regression rate in the axial direction is a nearly linear function of chamber pressure with a pressure exponent of 0.996.

Keywords: hybrid rockets; stabilized combustion; regression characteristics

1. Introduction

Recently, engineers and researchers have turned their attention to developing hybrid rocket motors for their numerous advantages over liquid bi-propellant and solid rocket motors. Because the fuel and oxidizer are physically separated and stored in different phases, hybrid rocket motors are considerably safer than their counterparts. Furthermore, hybrid rockets require only one feed system, which equates to greater reliability than liquid bi-propellant motors for throttling, thrust control, manoeuvring, motor shutdown, and restart.

∗Corresponding author, Ph.D. Student, E-mail: yuji.s@frontier.hokudai.ac.jp
[a]Professor, E-mail: nagata@eng.hokudai.ac.jp
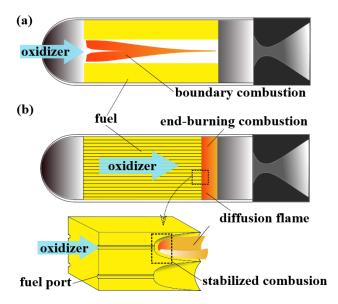
Yuji Saito et al.

Fig. 1 (a) Schematic of a conventional hybrid rocket and (b) axial-injection end-burning hybrid rocket

Fig. 1(a) shows a conventional hybrid rocket configuration. The conventional configuration commonly consists of a solid phase tubular fuel and a liquid phase oxidizer. Oxidizer passes through the solid fuel port and combustion occurs in this port as a boundary-layer combustion. Hybrid rocket development up to now has exposed several weak points, one of the most important being a ξ (oxidizer to fuel mass ratio) shift during firing and throttling (Chiaverini and Kuo 2007). Although throttling capability is a virtue of hybrid rockets, the accompanying ξ shift results in a loss of specific impulse and potential increase in residual propellant weight (Barato *at el.* 2014). In fact, even without any throttling, ξ tends to increase during firing as the fuel port diameter increases and the regression rate decreases.

To overcome this defect, Nagata *et al.* (1997) proposed an axial-injection end-burning hybrid rocket. Fig. 1(b) shows the basic idea. A key point of this idea is that a motor uses a cylindrical fuel with an array of many small ports running in the axial direction, through which oxidizer gas flows. A diffusion flame stabilizes at each port exit. The burning surface area changes with time just after ignition due to a micro-flame at each port exit propagating upstream. Because each port exit expands with time, neighbouring ports eventually merge with one another. After this initial transient, no ξ shift occurs during firing because the burning surface area no longer changes.

The first researchers to pursue an axial-injection end-burning hybrid rocket were Kato *et al.* (2001), Hashimoto *et al.* (2001), who carried out experimental investigations on the combustion of tobacco-filter-like fuel, in which oxidizer gas flows through the gaps of a fibrous fuel bed. They reported that when oxidizer velocity exceeded the blow-off limit, a flame stabilized at the end of the fuel, and that the flame's traveling velocity i.e. regression rate depends on chamber pressure. Because this regression characteristic is similar to that of solid rockets, they calculated the regression rate as a function of pressure as opposed to a function of propellant mass flow density, the approach commonly used for hybrid rockets. Their results indicated that the pressure exponent is almost 0.85, and they also reported that this axial-injection end-burning hybrid rocket has the potential to obtain good thrust characteristics.
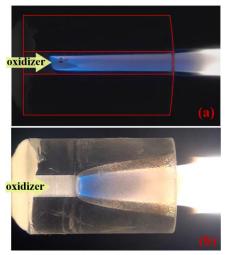
Fig. 2 Typical images of flames in a 3.0 mm diameter PMMA tube, where red lines outline the fuel shape (a) a common flame spreading combustion in oxidizer velocity 7.8 m/s, (b) a stabilized combustion in oxidizer velocity 25 m/s

Hashimoto and Nagata (2004) proposed an axial-injection end-burning hybrid rocket using stabilized combustion (Hashimoto *et al.* 2006) in a port of PMMA fuel. Fig. 2 compares stabilized combustion and common flame spreading combustion in a PMMA tube fuel similar to that used in their research.

Above a certain oxidizer velocity, stabilized combustion is achieved and the flame works to enlarge the local port exit surface. This stabilized combustion mode ensures that port exits merge with one another as shown in Fig. 1(b), and burning area remains constant. The velocity of the flame traveling against the oxidizer flow corresponds to the regression rate of the axial-injection end-burning hybrid rockets. By studying combustion characteristics of a single port fuel under varying chamber pressure, Hashimoto and Nagata (2004) revealed that the regression rate depends on the chamber pressure according to Eq. (1)

$$V_f = \left(\frac{C_1}{V_o} + C_2 \right) P^n ,$$

(1)

where $C_1 = 1.34 \times 10^{-7}$, and $C_2 = 1.61 \times 10^{-9}$ are constants, V_f [mm/s] is the regression rate in the axial direction, V_o [m/s] is the oxidizer velocity in a port and P_c [Pa] is the chamber pressure. The pressure exponent n is given by them to be close to unity (=0.951). This means virtually no ξ shift occurs during throttling. Although they attempted to conduct firing tests of a laboratory scale motor, they were unable to obtain stable end-burning regression. Based on these trials, they explained three requirements for a successful axial-injection end-burning motor: 1) high fuel filling rate for obtaining an optimal ξ; 2) small port intervals for increasing port merging rate; 3) ports arrayed across the entire fuel section. Because the manufacturing technology at that time was insufficient to produce a motor which satisfied these requirements, their research progress came to a halt.

Recently, Li *et al.* (2015) reported an axial-injection end-burning mode obtained in static firing tests with a laboratory scale motor. However, their understanding of "axial-injection end-burning"
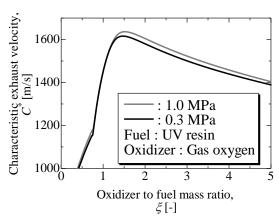
Fig. 3 C^*_{th} as a function of ξ

is different from the one suggested by Hashimoto and Nagata (2004). The axial-injection end-burning mode in their paper does not have the virtues of the one discussed in this paper, such as the outstanding throttling characteristics. Since there were too few ports and the port interval was too large, their opposed propagating mode, corresponding to our original idea, could not reach a steady state. Matthew *et al.* (2015) investigated experimentally and analytically the regression characteristics of axial-injection end-burning hybrid rocket fuels using 15-100 micron port diameter porous fuel rods. They conducted combustion experiments under varying chamber pressures and observed the regression rate. Their results indicated that the regression rate is a function of chamber pressure and its exponent *n* is close to unity. Additionally, they attempted to model the regression of axial-injection end-burning hybrid fuel using their experimental data and the Granular Diffusion Flame model. Although their study recreated the end burning regression characteristics achieved by Hashimoto and Nagata (2004), the fuel grain did not satisfy the requirement of high fuel filling rate.

Recent progress in 3D printing changed the situation; it is now possible to make any shape of solid fuel. Nagata *et al.* (2015) used this high accuracy 3D printer technology to satisfy the three requirements previously mentioned. From experimental data, they showed that no ξ shift occurred during firing, but they did not report on the regression characteristics. Until now, there had been no investigation on regression characteristics of an axial-injection end-burning fuel that has an array of small ports and satisfies the requirement for high fuel filling rate. Additionally, the good throttling characteristics indicated by single port experiments (Hashimoto and Nagata 2004) had not been confirmed by the static firing test of a motor. This paper analyses experimentally obtained regression rate and validates the outstanding throttling capability of axial-injection end-burning hybrid fuels having numerous small ports by a laboratory scale motor for the first time.

2. Material and methods

2.1 Fuel grain

The fuel grains are manufactured by a high precision light polymerized 3D printer. The fuel material is an ultraviolet curable resin consisting of 80% to 90% acrylic acid ester, 5%

hexamethylene acrylate, and photopolymerization initiator. Diameter and length of the fuel grain are 20 mm and 50 mm, respectively. The grain is composed of an array of 85 ports that are 0.3 mm in diameter at 2.0 mm intervals. As a result, a high fuel filling rate of 98.1% is attained. All fuel grains satisfied the three requirements given above for the axial-injection end-burning hybrid rockets.

All fuels were inspected by passing a 0.009 gauge (diameter 0.229 mm) guitar string through each port. Fuel port accuracy is discussed in section 3.2. The fuel diameter D [mm] was measured using a digital slide gauge before firing. The average fuel diameter was 19.8 mm and the standard deviation was 0.04 mm. This error corresponds to a 1.14 mm^2 standard deviation for area.

The theoretical characteristic exhaust velocity C^*_{th} [m/s] for this fuel was calculated by CEA code (Gordon and McBride 1994) and was employed for data reduction. Fig. 3 shows C^*_{th} as function of ξ at chamber pressures 0.3 MPa and 1.0 MPa.

2.2 Experimental setup

In total, the results of twelve firing tests, labelled test-1 to 12, are analysed in the following section. Fig. 4 shows the outline of the experimental apparatus used. It mainly consists of an oxygen tank, a nitrogen tank and a combustion chamber. There are 3 oxidizer lines with solenoid valves, needle valves and non-return valves for flow/non-flow control, controlling gas flow rate and preventing return flow of gas, respectively. The oxidizer flow timing was controlled by LabVIEW7. A digital video camera monitors the exit of the exhaust nozzle.

The oxidizer mass flow rate through the needle valve was measured by a mass flow meter before each firing. The mass flow meter used was a CMS200 (azbil) and the sensor error was plus/minus 3% of measured value plus one digit (2.2×10^{-2} g/s). Pressures upstream of the mass flow meter, fuel, and nozzle were measured as shown in Fig. 4. The chamber pressure was measured using PBH-A-2MP (Kyowa) and the sensor error was plus/minus 0.00104 MPa. Fuel weight was measure by using an Fz-300i (AND) electric scale with an accuracy of plus/minus 0.010 g.

Fig. 5 shows a schematic of the test motor. Oxygen flows into the combustion chamber from the left and enters the fuel grain from the left end face. The nozzle is a sonic type with an inner diameter of 2.5 mm in all tests. Fig. 5 also shows how the end face of the fuel grain is ignited. To

① Oxygen tank ⑥ Combustion chamber
② Nitrogen tank ⑦ Pressure sensor
③ Solenoid valve ⑧ Mass flow meter
④ Needle valve ⑨ Pressure relief valve
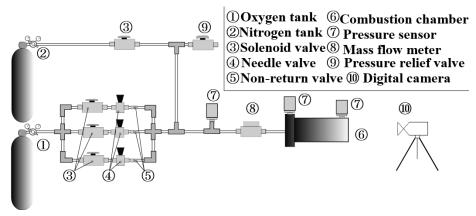⑤ Non-return valve ⑩ Digital camera
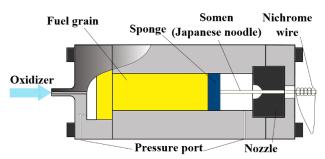
Fig. 4 Experimental apparatus

Fig. 5 Test motor and ignition method

prevent the nozzle from clogging, Somen is used as a fuse. While feeding oxygen into the engine at a low rate (about 2.2×10^{-2} g/s), the Somen is ignited by heating a Nichrome wire, and the resulting flame spreads into the chamber through the nozzle. Because it is important to ignite the entire end surface at once, a sponge is placed in front of the fuel grain end. When smoke is detected coming from the nozzle, the flame from the Somen has reached the Sponge. At this point, the gas oxygen feed is increased to a mid-operating level (0.3 g/s). This procedure plays an important role in ensuring ignition of the entire end surface, and thus in preventing back-firing through a port. After 5 s of operation, the oxygen supply is increased to a high-operating level. The entire procedure described above is controlled through the LabVIEW controlled needles.

2.3 Data reduction

To obtain the history of ξ during firing, the data reduction method explained below is employed (Nagata *et al*. 2014). This data reduction method uses chamber pressure, oxidizer mass flow rate, and total fuel consumption as input data. NASA's CEA code (Gordon and McBride 1994) was used to calculate C^*_{th} employing the "infinite area combustor" model with the shifting-flow assumption. Experimental data was filtered by 10-period running averages and used as input data for the reconstruction technique. Therefore, the original time resolution of 200 Hz reduced to 20 Hz.

By introducing the efficiency of characteristic exhaust velocity $\eta[-]$, which we assume to be constant during firing, we can obtain the following equation

$$\eta \, C^*_{th}\left(P_c, \xi\right) = \frac{P_c A_t}{\dot{m}_o\left(1 + 1/\xi\right)} \tag{2}$$

Here, $\dot{m}_o$ [kg/s] is oxidizer mass flow rate and A_t [m^2] is nozzle throat area.

By assuming a value for η, we can use Eq. (2) to calculate ξ. The bisection method with a stopping criterion of 10^{-6} convergence was employed to solve the equation. We call this method "RT-1," and denoted values obtained by this method with subscript 1 "ξ_1" to avoid confusion. Using this method, we encountered the problem of multiple solutions, reported by Nagata *et al*. (2014). As a result of the multiple solutions, we obtained a highly fluctuating ξ_1 history. Fig. 6 shows chamber pressure in red, and ξ as calculated by RT-1 in grey for test-5, which encountered the multiple solution problem. The value of ξ_1 has large fluctuations which do not coincide with chamber pressure history. In an effort to avoid this multiple solution region, we made a new calculation method called "RT-2".
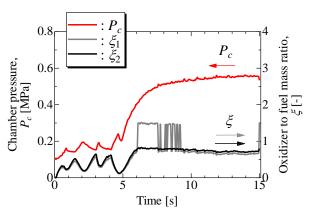
Fig. 6 A fluctuating (ξ_1) and an improved (ξ_2) history of ξ test-5

First, we calculate the average characteristic exhaust velocity C^*_{ave} [m/s] during firing

$$C^*_{ave} = \frac{\int_0^{t_f} P_c A_t dt}{\int_0^{t_f} \dot{m}_o dt + M_f} \tag{3}$$

where M_f [kg] is fuel consumption and t_f [s] is firing duration.

Assuming that the temporal characteristic exhaust velocity is C^*_{ave}, we can calculate ξ' according to Eq. (4)

$$\xi' = \frac{\dot{m}_o C^*_{ave}}{P_c A_t - \dot{m}_o C^*_{ave}} \tag{4}$$

Inputting ξ' into the CEA code, and assuming η and ξ are related according to Eq. (5), we solve the equation for ξ. This method allows us to avoid the convergent calculation from Eq. (2), meaning that Eq. (5) can overcome the difficulty of obtaining ξ when we encounter the multiple solution problem (the black solid line in Fig. 6 as ξ_2).

$$\xi = \frac{\dot{m}_o \eta\, C^*_{th}(P_c, \xi')}{P_c A_t - \dot{m}_o \eta\, C^*_{th}(P_c, \xi')}, \tag{5}$$

After obtaining ξ, the fuel mass flow rate $\dot{m}_f$ [kg/s] is determined by Eq. (6). The regression rate is then calculated by substituting $\dot{m}_f$ into Eq. (7), where ρ_f is fuel density ($=1191$ kg/m^3), A_f [m^2] is fuel area and a [-] is fuel filling rate.

$$\dot{m}_f = \frac{\dot{m}_o}{\xi}, \tag{6}$$

$$V_f = \frac{\dot{m}_f}{\rho_f A_f a}, \tag{7}$$

Integrating Eq. (6) gives the overall fuel mass consumption during firing $M_{f,cal}$ [kg]

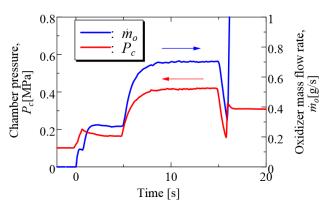$$M_{f,cal} = \int_0^{t_f} \dot{m}_f dt = \int_0^{t_f} \frac{\dot{m}_o}{\xi} dt \tag{8}$$

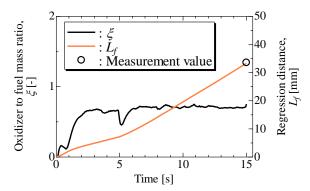Fig. 7 Measured histories of chamber pressure and oxidizer mass flow rate in test-8

Fig. 8 Calculated histories of ξ and L_f and measured L_f in test-8

The value of η is adjusted so that $M_{f,cal}$ agrees with the experimental value M_f.

$$M_{f,cal}(\eta) - M_f = 0 \tag{9}$$

Since this reconstruction technique, RT-2, avoids the multiple solutions problem, ξ_2 has a smaller fluctuation than ξ_1. Refer to Appendix-A for a detailed discussion of RT-2.

3. Results and discussion

3.1 Firing results

Fig. 7 shows chamber pressure and oxidizer mass flow rate histories in test-8. As previously mentioned, an ignition and supply sequence lasting 5 seconds is employed to ensure complete end surface ignition. Following this sequence, a steady state oxidizer mass flow rate is set, and chamber pressure in turn increases to a steady state value. After an overall initial transient of about 10 seconds, chamber pressure is maintained at an almost constant value. Fig. 8 shows the ξ history and regression distance L_f [m] obtained by RT-2, where L_f is calculated by integrating the regression rate over time.

Fig. 9 shows the fuel grain after firing in test-8. Fig. 9 (a) shows the comparison of the fuel
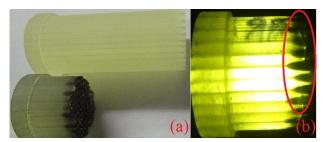
Fig. 9 Fuel grain after firing in test-8 (a) Comparison before and after firing, (b) Port regression

Table 1 Firing results

Test index	$\dot{m}_o^*$ [g/s]	P_c^* [MPa]	M_f [g]	t_f [s]	ξ^* [-]	V_f^* [mm/s]	V_o^* [m/s]	$B_{\dot{m}_o}$ [g/s]	B_ξ [-]	B_{V_f} [mm/s]	B_{V_o} [m/s]
1	0.55	0.29	10.86	20.0	0.87	1.76	24.1	3.9×10^{-2}	6.1×10^{-6}	1.2×10^{-1}	2.1
2	0.72	0.40	9.03	11.5	0.76	2.64	22.7	4.3×10^{-2}	1.1×10^{-5}	1.6×10^{-1}	1.8
3	0.48	0.27	6.46	14.8	0.62	2.13	22.4	3.6×10^{-2}	9.1×10^{-6}	1.6×10^{-1}	2.0
4	0.86	0.50	11.99	15.0	0.84	2.87	22.0	4.8×10^{-2}	4.2×10^{-6}	1.6×10^{-1}	1.6
5	0.93	0.52	15.11	15.0	0.76	3.38	22.3	5.0×10^{-2}	8.8×10^{-6}	1.8×10^{-1}	1.6
6	0.53	0.30	11.02	20.0	0.88	1.68	22.6	3.8×10^{-2}	2.7×10^{-5}	1.2×10^{-1}	2.0
7	0.79	0.47	11.73	15.0	0.79	2.79	21.4	4.6×10^{-2}	2.5×10^{-6}	1.6×10^{-1}	1.6
8	0.68	0.41	12.01	15.0	0.71	2.67	21.3	4.3×10^{-2}	1.1×10^{-5}	1.7×10^{-1}	1.7
9	0.84	0.49	13.71	13.0	0.69	3.34	21.5	4.7×10^{-2}	2.1×10^{-6}	1.9×10^{-1}	1.6
10	0.42	0.25	13.4	25.0	0.84	1.41	21.2	3.5×10^{-2}	8.3×10^{-6}	1.2×10^{-1}	2.0
11	0.93	0.60	16.93	17.9	0.63	4.10	19.7	4.5×10^{-2}	1.0×10^{-6}	2.2×10^{-1}	1.4
12	0.81	0.48	12.09	15.0	0.70	3.20	21.1	4.6×10^{-2}	7.1×10^{-6}	1.9×10^{-1}	1.6

*Average value during the steady state region of firing test

before and after firing. Note that regression seems to occur only at the end surface of the fuel. Fig. 9(b) shows port regression in detail using backlighting. It can be observed that each port end regresses into a tulip shape. During regression, the ports maintain this tulip shape as they merge with one another, hence the mechanism from which burning area is kept constant. From the results as shown in Figs. 8 and 9, we can recognize the axial-injection end-burning combustion mode for test-8.

Table 1 shows all test firing results; $\dot{m}_o$, P_c and ξ are expressed as the average of their steady state values. The oxidizer velocity in a port V_o [m/s] is determined by Eq. (10)

$$V_o = \frac{\dot{m}_o RT}{P_c A_f (1-a)}, \tag{10}$$

where R is the specific gas constant for oxygen (=260 J/(kg K)), and T is the temperature(=293 K). According to Table 1, the oxidizer to fuel ratio ξ in each test was around 0.8, which is far from the optimum value of around 1.5 corresponding to maximum C^* in Fig. 3. The reason for this discrepancy is that the fuel grains were designed for optimum ξ according to Eq. (1), which was derived for single port fuel grains. Values much lower than this optimum were observed in the

actual experiments, meaning that the regression rate of axial-injection end-burning hybrid rockets is higher than predictions made using Eq. (1). A detailed discussion of the regression rate is carried out in section 3.3.

3.2 Error analysis

To obtain an error bias for ξ, regression rate V_f (calculated by Eq. (7)), and oxidizer velocity V_o (calculated by Eq. (10)), an error analysis was performed according to the method introduced by Frederick and Greiner (1996). The error bias B_α for arbitrary test variable α is determined by Eq. (11), where x_i is the parameter for α, B_{xi} is the error bias for x_i parameter error, and $\partial\alpha/\partial x_i$ represents x_i sensitivity for α.

$$B_\alpha^{\,2} = \sum_i \left(\frac{\partial \alpha}{\partial x_i} B_{x_i} \right)^2 \tag{11}$$

Key experimental variables "α" and their functional parameters are defined by Eq. (12).

$$\xi = \xi\left(P_c, \dot{m}_o, M_f, A_t\right)$$
$$V_f = V_f\left(\xi, \dot{m}_o, a, A_f\right) \tag{12}$$
$$V_o = V_o\left(P_c, \dot{m}_o, a, A_f\right)$$

In these firing tests, A_t is not considered in the error analysis of ξ because nozzle erosion did not occur. We estimated the error bias of solving for ξ using the reconstruction technique by calculating ξ history when P_c, $\dot{m}_o$ and M_f are scaled 10%. The V_f and V_o bias were calculated using Eq. (7) and Eq. (10). Additionally, we have to consider the accuracy of the 3D printing process when determining fuel filling rate a. To do so, we estimated a using Eq. (13)

$$a = 1 - \sqrt{\frac{128\, N\, L\mu\, Q}{\Delta P \pi\, D^4}} \tag{13}$$

where N is the number of ports, L is fuel length (almost 50 mm), μ is viscosity coefficient of oxygen (=1.92 Pa s), Q is volumetric flow rate (almost 3.3×10^{-4} m^3/s) and ΔP [Pa] is pressure loss. Eq. (13) comes from the relation for the pressure loss in laminar pipe flow. The derivation of Eq. (13) is explained in Appendix-B. We removed the nozzle from the experimental apparatus depicted in Figs. 4 and 5, and measured chamber pressure upstream of the fuel for varying oxidizer flow. Nine tests for a estimation were conducted. The results showed that the average filling rate a was 98.1% and the standard deviation for a was 0.4%. Therefore, the error bias of a, B_a is 0.4%.

Table 1 also shows the error bias for each value, where $B_{\dot{m}_o}$, B_ξ, B_{V_f}, and B_{V_o} are the error biases of $\dot{m}_o$, ξ, V_f, and V_o, respectively. As mentioned earlier, the error bias for P_c, M_f and A_f is 0.00104 MPa, 0.01 g and 1.14 mm^2, respectively.

3.3 Regression characteristics

To investigate the regression characteristics, we conducted several firing tests with various oxidizer mass flow rates and chamber pressures as shown in Table 1. As can be seen in Fig. 1, the regression characteristic of an axial-injection end-burning hybrid rocket is very different than that
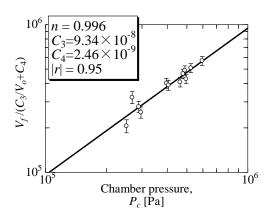
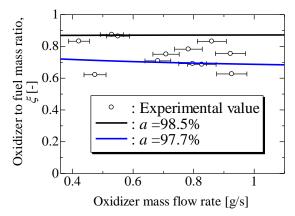Fig. 10 Effect of chamber pressure on regression rate

Fig. 11 Effect of oxidizer mass flow rate on ξ and theoretical calculation

of a conventional hybrid rocket. Whereas a conventional hybrid rocket has a regression rate that is a function of the propellant mass flow density, the axial-injection end-burning hybrid tested here has a regression rate that is a function of the chamber pressure. This tendency was recognized by Hashimoto and Nagata as suggested by Eq. (1) (Hashimoto and Nagata 2004). Additionally, the oxidizer velocity in a port influences regression rate. As mentioned in section 3.1, the oxidizer velocity varied for all tests. Therefore, we determined the regression rate using Eq. (14).

$$V_f = \left(\frac{C_3}{V_o} + C_4 \right) P^n \tag{14}$$

Fig. 10 shows the test results. The error bars in the figure come from the error analysis as explained in section 3.2. The trend line shown in the figure was fitted to the data using the least squares method, and the resulting pressure exponent n is thereby found to be 0.996; $C_3 = 9.34 \times 10^{-8}$, and $C_4 = 2.64 \times 10^{-9}$. This pressure exponent n is close to the value of 0.951 reported by Hashimoto and Nagata using PMMA fuels (Hashimoto and Nagata 2004), as well as the value of 1.05 reported by Matthew and Frederick (2015) using polyethylene fuels. All of these findings lead to the conclusion that regression rate for axial-injection end-burning hybrid rockets depends on

pressure, and the pressure exponent is close to unity.

The fact that n is close to unity means that ξ does not shift during throttling operation. Fig. 11 clearly shows this virtue. In Fig. 11, the horizontal and vertical axes are the oxidizer mass flow rate and ξ, respectively. The error bars come from the error analysis as explained in section 3.2. To confirm the validity of the observed regression rates, we calculated regression rate using Eq. (14). Fig. 11 shows the calculated results as solid lines. Using Eqs. (2), (6), (7), (10), (14) and the CEA code (Gordon and McBride 1994), we calculated ξ at each oxidizer mass flow rate and fuel filling rate. As mentioned in section 3.2, the fuel filling rate a varied due to the manufacturing accuracy for the fuel grain. Therefore, we consider a range for a from 97.7% to 98.5% corresponding to the error bias of 0.4% error at the averaged value 98.1%. In Fig. 11, with the exception of two points, all values fall within one standard deviation as determined according to error bias B_a. These results show no clear trend for the effect of oxidizer mass flow rate on ξ. In turn, this lack of sensitivity supports the claim that axial-injection end-burning hybrid rockets have good throttling characteristics. In other words, during a throttling process, ξ stays at a nearly constant value.

4. Conclusions

For the first time, a laboratory scale motor was used to analyse the regression characteristics and verify the throttling capability of axial-injection end-burning hybrid fuels having numerous small ports. High accuracy 3D printing allows for the production of fuel that satisfies the requirements for axial-injection end-burning hybrid rockets as defined in this paper. An instantaneous oxidizer to fuel mass ratio ξ was calculated using a new data reduction method, and found to remain nearly constant during firing. The regression rate in the axial direction depended on pressure with an exponent of 0.996. Results from firing tests show that ξ remains almost constant regardless of the value of the oxidizer mass flow rate, and confirm that axial-injection end-burning hybrid rockets exhibit superb the throttling characteristics.

Acknowledgements

References

Barato, F., Grosse, M. and Bettella, A. (2014), "Hybrid rocket fuel residuals-an overlooked topic", *Proceedings of the 50th AIAA/SAE/ASEE Joint Propulsion Conference*, Cleveland, USA, July.

Chiaverini, M.J. and Kuo, K.K. (2007), *Fundamentals of Hybrid Rocket Combustion and Propulsion*, American Institute of Aeronautics and Astronautics, Reston, USA.

Frederick, R.A. and Greiner, B.E. (1996), "Laboratory-scale hybrid rocket motor uncertainty analysis", *J. Propuls. Pow.*, **12**(3), 605-611.

Gordon, S. and McBride, B.J. (1994), "Computer program for calculation of complex chemical eEquilibrium", NASA Reference Publication, RP-1311.

Hashimoto, N. (2004), "End-burning type hybrid rocket", Ph.D. Dissertation, Hokkaido University,

Sapporo, Japan.

Hashimoto, N., Kato, T., Nagata, H., Akiba, R. and Kudo, I. (2001), "A preliminary study of end-burning hybrid rocket, Part 2: Combustion characteristics", *J. JPN Soc. Aeronaut. Space Sci.*, **49**(565), 40-47.

Hashimoto, N., Nagata, H., Totani, T. and Kudo, I. (2006), "Determining factor for the blowoff limit of a flame spreading in an opposed turbulent flow in a narrow solid-fuel duct", *Combus. Flame*, **147**(3), 222-232.

Hitt, M.A. and Frederick, R.A. (2015), "Testing and modeling of a porous polyethylene axial-injection end-burning hybrid rocket motor", *Proceedings of the 51st AIAA/SAE/ASEE Joint Propulsion Conference*, Orlando, USA, July.

Kato, T., Hashimoto, N., Nagata, H., Akiba, R. and Kudo, I. (2001), "A preliminary study of end-burning hybrid rocket, Part 1: Combustion stability", *J. JPN Soc. Aeronaut. Space Sci.*, **49**(565), 33-39.

Li, X.T., Tian, H., Yu, N. and Cai, G.B. (2015), "Experimental investigation of combustion in axial-injection end-burning hybrid rocket motor", *J. Propuls. Pow.*, **31**(3), 930-936.

Nagata, H., Nakayama, H., Watanabe, M., Wakita, M. and Totani, T. (2014), "Accuracy and applicable range of a reconstruction technique for hybrid rockets", *Adv. Aircraft Spacecraft Sci.*, **1**(3), 273-289.

Nagata, H., Okada, K., Sanda, T., Kato, T., Akiba, R., Satori, S. and Kudo, I. (1997), "Combustion characteristics of fibrous fuels for dry towel hybrid rocket motor", *J. Space Technol. Sci.*, **13**(1), 11-16.

Nagata, H., Teraki, H., Saito, Y., Kanai, R., Yasukochi, H., Wakita, M. and Totani, T. (2015), "Verification firings of end-burning type hybrid rockets", *Proceedings of the 51st AIAA/SAE/ASEE Joint Propulsion Conference*, Orlando, USA, July.

EC

Nomenclature

a	=	fuel filling rate
A_t	=	nozzle throat area
A_f	=	fuel area
B	=	error bias defined by Eq. (11)
C_1	=	constant value used in Eq. (1)
C_2	=	constant value used in Eq. (1)
C_3	=	constant value used in Eq. (14)
C_4	=	constant value used in Eq. (14)
C^*_{th}	=	theoretical characteristic exhaust velocity used in Eq. (2)
C^*_{ave}	=	average characteristic exhaust velocity defined by Eq. (3)
d	=	port diameter in fuel diameter
D	=	fuel diameter
L	=	fuel length
L_f	=	regression distance
$\dot{m}_o$	=	oxidizer mass flow rate
$\dot{m}_f$	=	fuel mass flow rate obtained by Eq. (6)
M_f	=	experimental fuel mass consumption during firing
$M_{f,cal}$	=	calculating fuel mass consumption during firing obtained by Eq. (8)
n	=	pressure exponent
N	=	number of port

Q = volumetric flow rate used in Eq. (13)
P_c = chamber pressure
R = specific gas constant for oxygen (=260 J/(kg K))
T = temperature (=293 K)
t_f = firing duration
V_o = oxidizer velocity in a port obtained by Eq. (10)
V_f = regression rate for fuel obtained by Eq. (7)
ΔP = pressure loss used in Eq. (13)
η = efficiency of characteristic exhaust velocity
μ = viscosity coefficient of oxygen used in Eq. (13) (=1.92 Pa s)
ξ = oxidizer to fuel ratio obtained by Eq. (5) (=ξ_2)
ξ' = oxidizer to fuel ratio obtained by Eq. (4)
ξ_1 = oxidizer to fuel ratio obtained by Eq. (2)
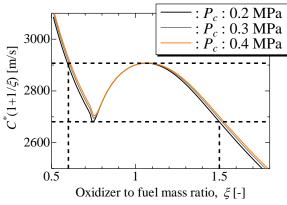ρ_f = fuel density (=1191 kg/m^3)

Appendix A. Multiple solution problem for reconstrustion technique

The reason there are multiple solutions to RT-1 can be explained by examining Eq. (A-1)

$$C^*_{th}(P_c, \xi)\left(1 + \frac{1}{\xi}\right) = \frac{P_c A_t}{\dot{m}_o}, \qquad (A-1)$$

which is simply Eq. (2) rearranged to show an expression for $C^*(1+1/\xi)$. The right hand side of Eq. (A-1) is known from experimental data, and thus the left hand side represents the calculation carried out in RT-1. The black, grey and orange solid lines in Fig. A1 show $C^*(1+1/\xi)$ as function of ξ at 0.2, 0.3 and 0.4 MPa, respectively. The comparison of these three lines in Fig. A1 reveals that $C^*(1+1/\xi)$ does not depend on pressure. In Fig. A1, a given value for $C^*(1+1/\xi)$ may correspond to multiple values of ξ in the region $0.5<\xi<1.5$. This is why the solutions for ξ determined by RT-1 may display large oscillations inconsistent with the observed chamber pressure history. The calculation method RT-2 can avoid this multiple problem because it uses Eq. (5) instead of Eq. (2). Equation (5) uses a pre-determined value for ξ obtained by Eq. (4), which uses an averaged C^* value as opposed to that determined using Eq. (2).

Fig. A2 shows the histories of $P_c A_t/\dot{m}_o$ and ξ in test-8. In Fig. A2, the orange line is $P_c A_t/\dot{m}_o$, and the solid grey and black lines are ξ determined by RT-1 (ξ_1) and RT-2 (ξ_2), respectively. The black dotted lines enclose the multiple solution range. The orange solid line in Fig. A2 falls beneath the upper black dotted line in multiple instances between 8 and 13 seconds in firing. When this happens, the grey solid line (ξ_1) rapidly increases as Fig. A2 shows. This behaviour clearly shows the difficulty of obtaining ξ in the multiple solution range using RT-1. On the other hand, the ξ_2 history does not have fluctuations like that of ξ_1, demonstrating that RT-2 can avoid the multiple problem as previously mentioned. As can be seen in Fig. A2, when the orange solid lies outside of the multiple solution range, ξ_2 closely follows ξ_1. Therefore, we can use RT-2 to overcome the difficulty of determining ξ in the multiple solution region with an acceptable level of uncertainty. A full investigation of the accuracy of RT-2, such as that reported by Nagata *et al.* (2014) for RT-1, is necessary but out of the scope of this paper.
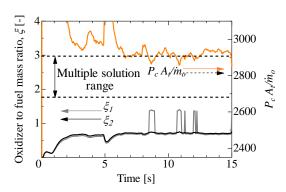

Fig. A1 Relationship $C^*(1+1/\xi)$ vs. ξ

Fig. A2 History of $P_c A_t/\dot{m}_o$, a fluctuating (ξ_1) ξ and an improved (ξ_2) ξ in test-8

Appendix B. The derivation of Eq. (13)

The pressure loss ΔP is expressed as follows

$$\Delta P = \rho_o \, \lambda \frac{L}{d} \frac{V_o^2}{2}, \tag{A-2}$$

where, λ is the resistance coefficient of a pipe. When the flow in the pipe is laminar, λ is expressed as follows

$$\lambda = \frac{64}{\mathrm{Re}} \tag{A-3}$$

where, Re is Reynolds number as determined by Eq. (A-4).

$$\mathrm{Re} = \frac{\rho_o V_o \, d}{\mu} \tag{A-4}$$

For Mach number Ma<0.3, the flow can be considered incompressible, and the oxidizer velocity in a port can be expressed as follows

$$V_o = \frac{Q}{\dfrac{\pi D^2}{4}(1-a)} \tag{A-5}$$

The fuel filling rate is defined as follows

$$a = 1 - N\left(\frac{d}{D}\right)^2 \tag{A-6}$$

By combining Eqs. (A-1) to (A-5), the estimation of fuel filling rate based on the governing equations for incompressible laminar pipe flow is expressed as Eq. (13).